PLOS COMPUTATIONAL BIOLOGY

RESEARCH ARTICLE

Hydrodynamics of transient cell-cell contact: The role of membrane permeability and active protrusion length

Kai Liu[1,2], **Brian Chu**[3], **Jay Newby**[4], **Elizabeth L. Read**[3,5], **John Lowengrub**[1,5], **Jun Allard**[1,5,6]*

1 Department of Mathematics, University of California Irvine, Irvine, California, United States of America, **2** Center for Mathematical Sciences, Huazhong University of Science and Technology, Wuhan, China, **3** Department of Chemical Engineering and Materials Science, University of California Irvine, Irvine, California, United States of America, **4** Department of Mathematics, University of Alberta, Edmonton, Alberta, Canada, **5** Center for Complex Biological Systems, University of California Irvine, Irvine, California, United States of America, **6** Department of Physics and Astronomy, University of California Irvine, Irvine, California, United States of America

* jun.allard@uci.edu

Citation: Liu K, Chu B, Newby J, Read EL, Lowengrub J, Allard J (2019) Hydrodynamics of transient cell-cell contact: The role of membrane permeability and active protrusion length. PLoS Comput Biol 15(4): e1006352. https://doi.org/10.1371/journal.pcbi.1006352

Editor: Anand R. Asthagiri, Northeastern University, UNITED STATES

Received: July 9, 2018

Accepted: February 1, 2019

Published: April 25, 2019

Data Availability Statement: All data are presented in the figures and Supporting Information.

Funding: This work was supported by National Science Foundation (nsf.gov) grant DMS 1454739 to JA, National Science Foundation grant DMS 1715455 to ELR, National Science Foundation grant DMS 1763272 to JA and JL, and a grant from the Simons Foundation (www.simonsfoundation.org) to JA and JL. The funders had no role in study design, data collection and

Abstract

In many biological settings, two or more cells come into physical contact to form a cell-cell interface. In some cases, the cell-cell contact must be transient, forming on timescales of seconds. One example is offered by the T cell, an immune cell which must attach to the surface of other cells in order to decipher information about disease. The aspect ratio of these interfaces (tens of nanometers thick and tens of micrometers in diameter) puts them into the thin-layer limit, or "lubrication limit", of fluid dynamics. A key question is how the receptors and ligands on opposing cells come into contact. What are the relative roles of thermal undulations of the plasma membrane and deterministic forces from active filopodia? We use a computational fluid dynamics algorithm capable of simulating 10-nanometer-scale fluid-structure interactions with thermal fluctuations up to seconds- and microns-scales. We use this to simulate two opposing membranes, variously including thermal fluctuations, active forces, and membrane permeability. In some regimes dominated by thermal fluctuations, proximity is a rare event, which we capture by computing mean first-passage times using a Weighted Ensemble rare-event computational method. Our results demonstrate a parameter regime in which the time it takes for an active force to drive local contact actually increases if the cells are being held closer together (e.g., by nonspecific adhesion), a phenomenon we attribute to the thin-layer effect. This leads to an optimal initial cell-cell separation for fastest receptor-ligand binding, which could have relevance for the role of cellular protrusions like microvilli. We reproduce a previous experimental observation that fluctuation spatial scales are largely unaffected, but timescales are dramatically slowed, by the thin-layer effect. We also find that membrane permeability would need to be above physiological levels to abrogate the thin-layer effect.

analysis, decision to publish, or preparation of the manuscript.

Competing interests: The authors have declared that no competing interests exist.

Author summary

The elastohydrodynamics of water in and around cells is playing an increasingly recognized role in biology. In this work, we investigate the flow of extracellular fluid in between cells during the formation of a cell-cell contact, to determine whether its necessary evacuation as the cells approach is a rate-limiting step before molecules on either cell can interact. To overcome the computational challenges associated with simulating fluid in this mechanically soft, stochastic and high-aspect-ratio environment, we extend a computational framework where the cell plasma membranes are treated as immersed boundaries in the fluid, and combine this with computational methods for simulating stochastic rare events in which an ensemble of simulations are given weights according to their probability. We find that the membranes fluctuate independently with a characteristic timescale of approximately microseconds, but that as the cells approach, a new, slower timescale of approximately milliseconds is introduced. Thermal undulations nor typical amounts of membrane permeability can overcome the timescale, but active forces, e.g., from the cytoskeleton, can. Our results suggest an explanation for differences in molecular interactions in live cells compared to in vitro reconstitution experiments.

Introduction

In many biological processes, two or more cells come into physical contact to form a cell-cell interface. These include cell-cell contacts like those in the epithelium [1, 2] that change on timescales of hours, and also transient contacts that form on seconds timescales, including those formed by lymphocytes and other immune cells that must interrogate many cells rapidly [3, 4]. A fundamental question for all cell-cell interfaces is how receptors and ligands come into contact, despite being separated by extracellular fluid, various large surface molecules like ectodomains of membrane proteins, and other structures in the negatively-charged glycocalyx. The contribution of large surface molecules has received most attention, for example producing spatial pattern formation based on molecular size [5–9] of the T cell receptor (TCR) and the immunotherapy target PD-1 [10]. In this work, we focus on the role of the fluid [11–14].

To highlight the potential importance of the hydrodynamics of extracellular fluid at an interface, we perform a preliminary calculation (unrealistically) assuming cells are rigid, impermeable spheres of radius r_{cell}. In order to bring these cells into close contact, a force F pushes them together, as shown in Fig 1A. This fluid dynamics problem can be solved analytically for the separation distance z, yielding [15, 16]

$$\frac{dz}{dt} = -\frac{1}{6\pi\eta r_{\mathrm{cell}}}\left(\frac{z}{r_{\mathrm{cell}}}\right)F \tag{1}$$

where η is the extracellular fluid viscosity. This equation is reminiscent of the Stokes drag formula for a sphere in free fluid, but modified by a factor $(z/r_{\mathrm{cell}}) \sim (10\ \mu\mathrm{m}/10\ \mathrm{nm}) \sim 10^3$. In other words, the force required to move two cells together is increased by a thousand-fold, a strikingly large correction. This observation, known as the "lubrication limit", "confinement effect" or "thin-layer effect" [11, 15, 16], heuristically arises because a small change in z requires incompressible fluid to move a large distance to outside the interface.

The cell surface is not a rigid sphere, but a deformable membrane subject to thermal undulations, active forces, and hydraulic permeability due largely to membrane inclusions like aquaporins. In this context, we ask, what is the role of the fluid in close-contact formation?

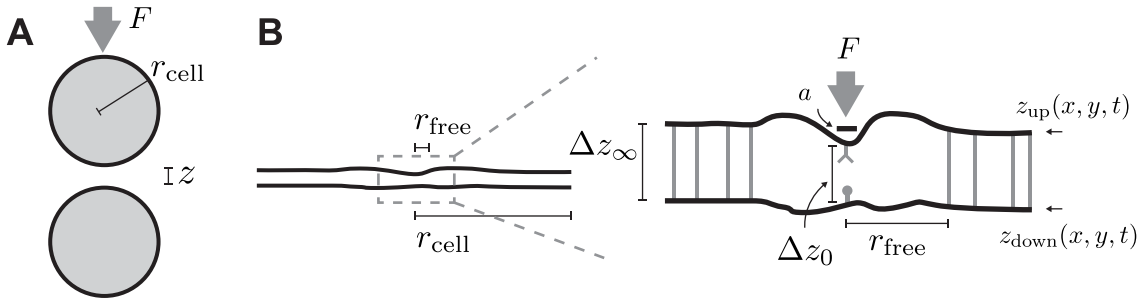

Fig 1. (A) Two cells, here depicted as spheres, pushed together by a force F. (B) Schematic of model geometry. Both cells have radius r_{cell} much larger than the cell-cell separation distance (left). We assume the cells are held apart by nonspecific adhesion molecules with size Δz_∞, which we refer to as the far-field separation. Near the receptor, there is a region free of nonspecific adhesion molecules of radius r_{free}, which is related to the surface density of non-specific adhesion molecules $\rho \approx 1/r_{\text{free}}^2$. The membrane separation distance at the receptor is Δz_0. In simulations with active forces, the force F is applied to a circular area of the top membrane with radius a.

https://doi.org/10.1371/journal.pcbi.1006352.g001

Are thermal undulations sufficient for receptor proximity? Are typical F-actin filopodial forces, ∼10 picoNewtons [17, 18], sufficient for receptor proximity? And how much force is required for rapid proximity (<1 second)? If there is a significant thin-layer effect, the force required will increase for smaller cell-cell distances, but larger distances require longer protrusions, suggesting the possibility of an optimal "attack range" which might explain the biological benefit of filopodia. If the membrane is permeable to extracellular fluid [19], how much permeability is required for rapid proximity? Factors that influence permeability, such as aquaporins, are under regulation [20], differentially localized, and impact cell processes including cancer angiogenesis [21], raising the possibility that cell-cell contact can be regulated in this way.

In contrast to previous theoretical studies of cell-cell interfaces, many of which capture membrane and molecular dynamics but exclude hydrodynamics, or exploit equilibrium statistical physics and therefore omit dynamics, studying the influence of active forces requires a full fluid dynamics model. Such models have been studied using both analytical methods [22, 23] and computational methods [24], reviewed in [25]. We have developed a computational fluid dynamics algorithm capable of simulating fluid-structure interactions with thermal fluctuations on seconds- and microns-scales [26] based on the Stochastic Immersed Boundary Method [24, 27–30]. Here, we use this to simulate two opposing membranes, variously including thermal fluctuations, active forces, and membrane permeability. We find that the thermal fluctuations are significantly modified by the thin-layer effect for a range of assumptions about molecular sizes. Active forces are sufficient to drive proximity. The thin-layer effect has the consequence of introducing two timescales (milliseconds and microseconds) in response to the two length scales inherent in the system. We find that membrane hydraulic permeability overcomes the thin-layer effects, but only for values larger than previous physiological estimates.

Results

Computational fluid dynamics simulation of the thin layer between cells

Receptor-ligand contact for the TCR occurs when the membranes are separated by $\Delta z_0^\star \approx 13$ nm. For the remainder of the manuscript, we refer to "membrane proximity" or "receptor-ligand contact", defined as membrane configurations with separation $\Delta z_0 \leq \Delta z_0^\star$. Other parts of the membranes are separated by a distance Δz_∞, where estimates range from 22 nm to 150 nm [7, 31–37] for ectodomains of signaling molecules like CD45, non-specific

binding pairs like LFA-ICAM and cadherins, and the glycocalyx. At the same time, cells themselves are $r_{cell} \sim 2\ \mu$m for the smallest T cells [3]. To explore the consequences of the thin layer geometry, plus the incompressibility of fluid, we are required to simulate a 3D system with a resolution of receptor-ligand size $\Delta z_0^\star$ in a domain larger than the cell, which has radius r_{cell}. (The analogous system in 2D would be insufficient since the opportunity for evacuating from the interface is fundamentally dependent on dimensionality of the boundary.)

The two cell surfaces are represented by elastic disks, as shown in Fig 1B, subject to bending resistance and approximate inextensibility. These disks are held by boundary tension σ_0 in their plane, and separated by approximately inextensible nonspecific molecules of size Δz_∞, which we refer to as the far-field separation. These non-specific adhesions are absent from a region of radius r_{free} around the center of the disk, which we identify as the site of the receptor. We assume both intracellular and extracellular fluids are Newtonian with viscosity of water, $\eta = 10^{-3}$ Pas. At the small length scales in our simulation, of ∼nm, the viscosity of the cytosol can be one or two orders of magnitude larger [38], and at large length scales in our simulation, the viscosity is even larger. The variability of viscosity, and its dependence on length scale of observation, is an active area of research and is attributed to the heterogeneous content of the cytoplasm and ordering of water [38]. (We do not *a priori* include here the concept of "effective viscosity" to describe the phenomenon of slower timescales due to fluid confinement [22], since we anticipate these emerge from the dynamics naturally.) Thus, all times we report are underestimates, and dynamics at more realistic viscosity and cell separation are expected to be slower. Due to the linear nature of the fluid dynamics equations we use, all times scale linearly with viscosity.

To simulate this model, we use an implementation of the Stochastic Immersed Boundary framework. We largely overcome the numerical challenges mentioned above, allowing us to simulate with parameters within the order-of-magnitude of experimentally estimated values, shown in Table 1. This framework, discussed in more detail in Methods and in the Supplemental Material, numerically approximates the fluid in an Eulerian representation, discretized in a rectangular Cartesian grid, while approximating the structure (in this case, the one or two membranes) in a Lagrangian representation, discretized as a triangulated mesh.

Thermal fluctuations are modulated by hydrodynamic dampening

As a control, we simulate a single membrane with thermal undulations, being held in place by adhesion molecules attached to fixed points in the fluid, as if it were attached to a "ghost" membrane. This simulation could be identified, for example, with a situation in which a cell is

Table 1. Model parameters.

Symbol	Name	Literature estimate & source	Value used here
r_{cell}	Cell radius	2 – 5 μm [3]	1 μm
r_{free}	LSM-free radius	∼ 100nm [6]	80 – 300nm
Δz_∞	Far-field separation, i.e., LSM height	22 – 150nm [7, 31–37]	30 – 120nm
$\Delta z_0^\star$	Critical separation for binding	13nm [39]	20nm
η	Viscosity	10^{-3} – 10^{-1} Pas [38]	10^{-3} Pas
B	Membrane bending modulus	50 pNnm [40]	50 pNnm
σ_0	Membrane (boundary) tension	0 – 100 pN/ μm [40, 41]	0 – 100 pN/ μm
F	Active force	1 – 100 pN [17, 18]	1 – 20 pN
a	Force radius	10 – 100nm [17, 42]	10nm
ψ	Membrane permeability	10^{-2} – 10^{1} nm/sPa [19, 38]	0 – 10^{4} nm/sPa

https://doi.org/10.1371/journal.pcbi.1006352.t001

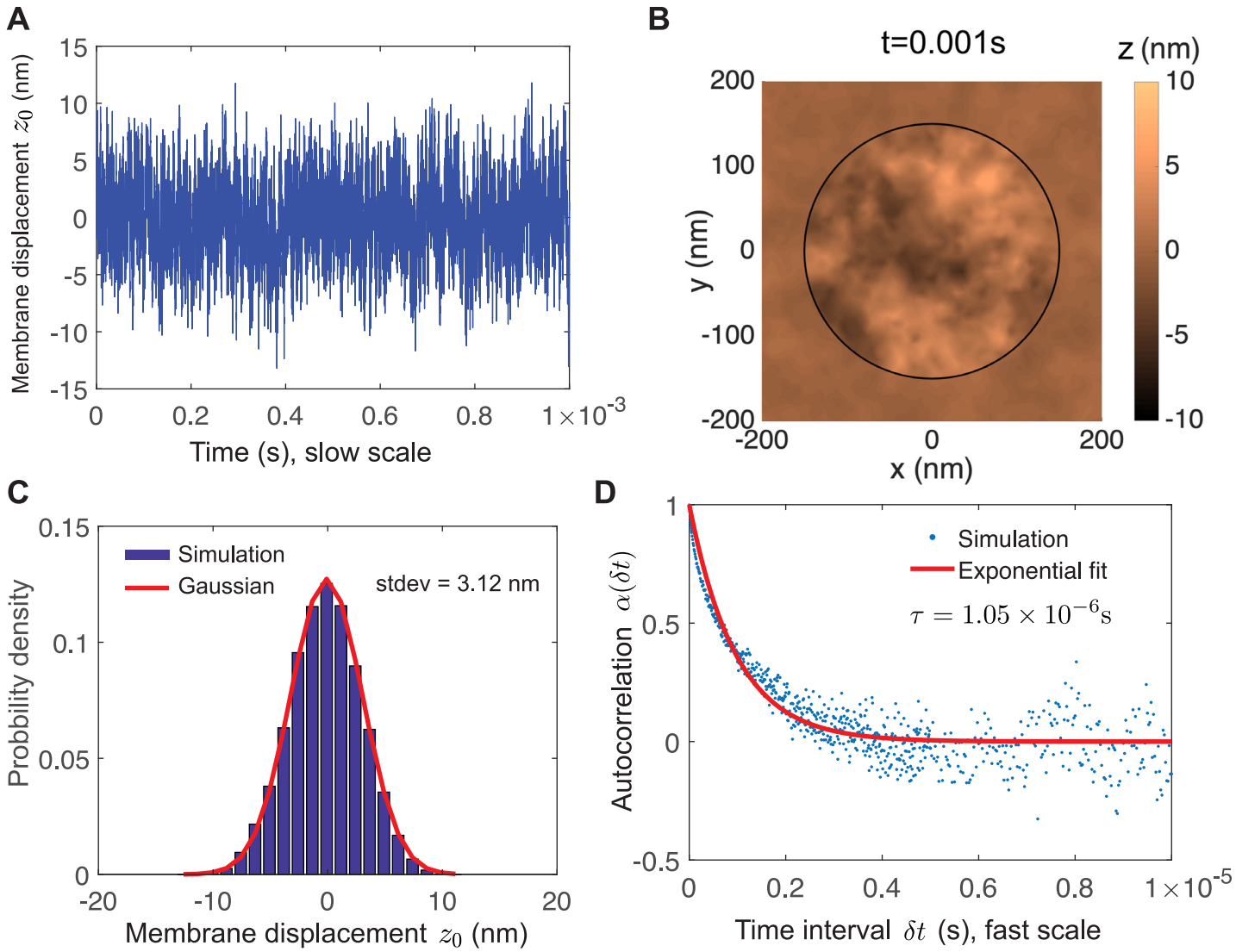

Fig 2. Thermal undulations of a single membrane. (A) Time series of membrane displacement at receptor coordinate $z_0(t)$. (B) Snapshot of membrane shape. For clarity, shown is a subset of the full simulation domain, which extends to $r_{cell} = 1$ μm. (C) Stationary probability of membrane displacement at receptor coordinate follows a Gaussian distribution with zero mean and standard deviation 3.12nm. (D) Autocorrelation $\alpha(\delta t)$ of membrane displacement at receptor coordinate is well-approximated by a single exponential decay, indicating a simple stochastic process, with timescale $\tau = 1.05 \times 10^{-6}$ s. Parameters used in this simulation are $r_{free} = 150$ nm, $\sigma_0 = 100$ pN/ μm.

https://doi.org/10.1371/journal.pcbi.1006352.g002

adhered to a highly permeable surface like a sparse network of extracellular matrix [43, 44] that provides minimal hydrodynamic confinement. A snapshot top view is shown in Fig 2B. We find that the position of the receptor fluctuates as a Gaussian with standard deviation $\sigma =$ 3.12nm (95% confidence interval [3.10, 3.15]nm) and an autocorrelation well-described by a single exponential decay with timescale $\tau = 1.05 \times 10^{-6}$ s (95% confidence interval [1.02, 1.08] $\times 10^{-6}$ s).

Dynamics (both deterministic and stochastic) of a single membrane can be decomposed into modes, each with a timescale that, in some geometries, can be solved for explicitly [23, 25]. The timescale of the nth mode associated with tension scales as $\eta r_{free}/\sigma_0\, n \sim 10^{-6}$ s/n, and that the nth mode associated with bending scales as $\eta r_{free}/Bn^3 \sim 10^{-8}$ s/n^3, although both with

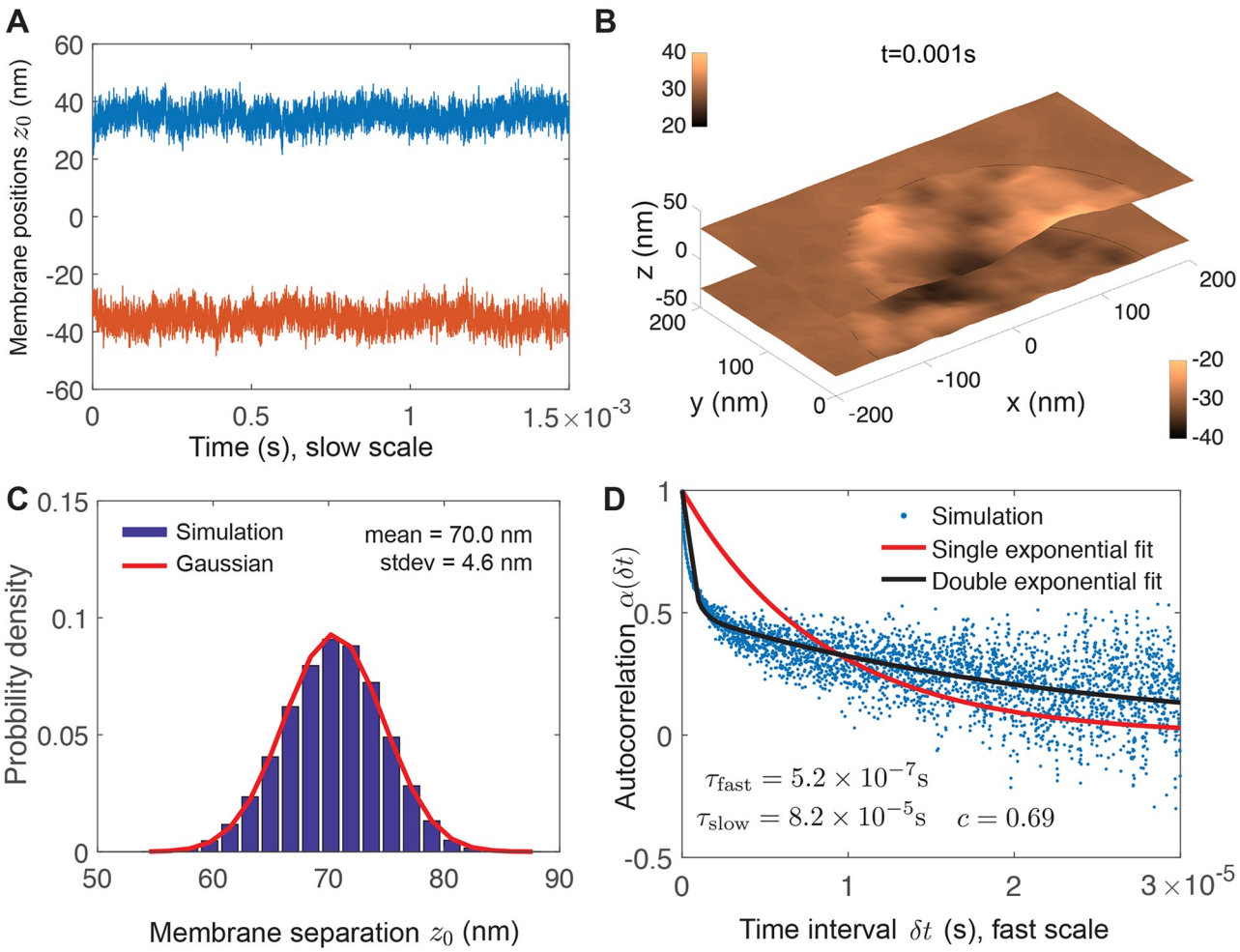

Fig 3. Thermal undulations of a cell-cell interface show thin-layer effect. Two membranes are held apart by Δz_∞ = 60nm. (A) Time series of membrane positions at receptor coordinate. (B) Snapshot of membrane shapes. (C) Stationary probability of membrane separation at receptor coordinate follows a Gaussian distribution with mean 70nm (larger than the far-field separation) and standard deviation 4.6nm. (D) Autocorrelation $\alpha(\delta t)$ of membrane separation does not fit a single exponential, but rather exhibits two timescales of decay, $\tau_{fast} = 5.2 \times 10^{-7}$ s and $\tau_{slow} = 8.2 \times 10^{-5}$ s, where a fraction $c = 0.69$ of the composite process is attributed to the slow process. Note different time axis in (D) compared to Fig 2D. Parameters used in this simulation are $r_{cell} = 1\ \mu$m, $r_{free} = 150$ nm, $\sigma_0 = 100$ pN/ μm.

https://doi.org/10.1371/journal.pcbi.1006352.g003

significant prefactors. Thus, our computational results are broadly consistent with the dominant mode being the first mode associated with tension.

We next simulate the interface with two membranes, as shown in Fig 3D. The membranes are held at Δz_∞ = 60nm outside the free radius. We run simulations for 1 s. We observe a stationary probability with mean separation $\langle \Delta z \rangle$ = 70.0nm. This blistering by 10nm is due to an entropic repulsive pressure arising from thermal fluctuations [23, 45, 46] and is not observed in simulations where thermal fluctuations are removed (shown below).

We observe a relatively small change in the amplitude of fluctuation compared to the single-membrane case, from 3.2nm to 4.6nm (95% confidence interval [4.5, 4.6]nm). The autocorrelation of Δz_0 does not fit a single exponential, but rather fits a two-timescale decay (black curve, Eq 21) with a fast timescale $\tau_{fast} = 5.3 \times 10^{-7}$ s (95% confidence interval $[5.0 - 5.4] \times 10^{-7}$ s) comparable to the single-membrane autocorrelation above, but also a slow timescale $\tau_{slow} = 8.2 \times 10^{-5}$ s (95% confidence interval $[8.1, 8.3] \times 10^{-5}$ s). The fraction of the autocorrelation function

described by the slow process is $c^2 = 0.48$ (95% confidence interval [0.43, 0.53]). The double exponential equation we use to fit the autocorrelation is not a perfect fit, reflecting the inherent complexity of this process and the need for such computational modeling. This finding is in agreement with previous experimental work [11, 23] showing that spatial amplitudes are not changed significantly, but fluctuation timescales are significantly altered by confinement.

We again compare the timescale with previous estimates for a similar case that has been previously studied: a membrane near a wall [23]. The timescale of the nth mode associated with tension scales as $\eta r_{\text{free}}^4/\sigma_0(\Delta z_\infty)^3 n^4 \sim 10^{-4}\,\text{s}/n^4$ (see Eq. 2.18 in [23]). Again, our computational results are broadly consistent with the dominant mode being the first mode associated with tension.

The timescales of thermal fluctuations are modified due to hydrodynamic dampening

Since the rate of receptor triggering is determined by the timescale of proximity (i.e., sufficient for close contact between receptor and ligand), we next want to use the fluid dynamics simulations to estimate the mean first-passage time (MFPT) to proximity. Since these simulations include the target ligand only implicitly, we can infer the mean time to proximity for several values of $\Delta z_0^\star$. For the simulations with $\Delta z_\infty = 60$nm, we ran fluid dynamics simulations for 1 second. For $\Delta z_0^\star = 13\,\text{nm}$, proximity of $\Delta z_0 < \Delta z_0^\star$ was not observed, suggesting it is a rare event in the sense that it occurs on a timescale much larger than the fluctuation timescale.

Computational expense prohibits us from simulating significantly longer times. To overcome this computational challenge of observing such rare close contacts, in this section, we develop an approximation based on Ornstein-Ulhenbeck (OU) processes [47], and then use the Weighted Ensemble [48, 49] computational method to find the mean first time to a particular state of the system, here defined as the first time for the membranes to be within a distance of $\Delta z_0^\star$ of each other. Full details are in Methods and S1 Appendix.

For the interface, we find that membranes will displace by 20 nm (i.e., the separation distance deviated from its mean of 70 nm down to 50 nm) in approximately 10^{-2} s. The time until a displacement larger than this grows super-exponentially: for a displacement of 25 nm (i.e., down to separation $\Delta z_0^\star = 45\,\text{nm}$), it takes $\sim$1 s.

For the single membrane case, an analytical approximation exists for the single-component OU [50], solid black line in Fig 4, allowing us to confirm our computational method (further validation is provided in S1 Appendix). In Fig 4, the interface case apparently has a larger (i.e., slower) MFPT for the single membrane. However, we note that these numbers are not directly comparable. The single-component OU describes the position of a single membrane, which has standard deviation $\sigma_1 = 3.1$ nm, while the two-component OU describes the distance between two membranes, which has a standard deviation $\sigma_2 = 4.6$ nm. A more direct comparison would be a hypothetical simulation in which two "single" membranes were held at a distance of 70 nm, but did not interact via fluid therefore would fluctuate independently. In such a case, the separation between these membranes would be $\sigma_{\text{indep}} = \sqrt{2\sigma_1^2} \approx 4.4\,\text{nm}$, approximately the same as the interface standard deviation.

Active forces from F-actin filopodia-like protrusions are significantly hampered by interface but still sufficient for rapid proximity

Cells, including the T cell, continuously extend active processes driven by F-actin like filopodia and microvilli [42, 51] that facilitate receptor binding [37, 52]. To explore the effect of hydrodynamics on active processes at an interface, we simulate a force F at the receptor site, spread over

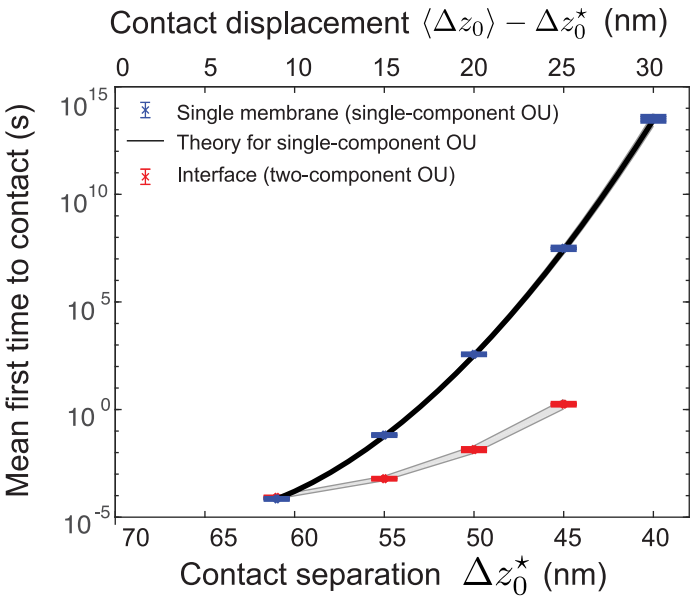

Fig 4. Estimation of mean first-passage time to proximity by approximating fluid dynamics with reduced stochastic process. The full fluid dynamics simulation produces parameters for single membrane and two membranes (Figs 2C, 2D and 3C, 3D, respectively) that are used to parametrize reduced Ornstein-Ulhenbeck models, which are then used to estimate mean first-passage time to separation distance $\Delta z_0^\star$. For a single membrane with parameters from Fig 2C and 2D, the MFPTs (blue) agree with theoretical results from [50]. For two membranes with parameters from Fig 3C and 3D, the MFPTs (red) increase super-exponentially. Error bars indicate ± one standard deviation of ten independent Weighted Ensemble runs. Gray shading indicates estimated 95% confidence interval based on uncertainty in the estimated OU parameters.

https://doi.org/10.1371/journal.pcbi.1006352.g004

a disk of radius $a = 10$ nm 1B. In Fig 5, we find that a force of $F = 20$ pN is sufficient to drive proximity from a far-field separation of $\Delta z_\infty = 50$ nm for both single membranes and interfaces.

We perform deterministic simulations with thermal forces omitted (black curves in Fig 5). The dynamics are quantitatively similar, and the simulations are much less computationally taxing. For this reason, for the remainder of this section we perform simulations without thermal fluctuations. Note in Fig 5 the stochastic and deterministic simulations approach equilibrium on approximately the same slow timescale, but the equilibrium separation is larger when thermal forces are included due to the entropic repulsion discussed above.

The shape of the protrusion is shown in Fig 5C and 5D. Membrane profiles are reminiscent of micrographs of microvilli in T cells (see, e.g., [37] Fig. 3G): The edges are rounded due to membrane bending resistance, and closest proximity is at the tip, with cell separation distance gradually tapering off.

To isolate the influence of the thin-layer effect, we perform identical simulations with and without a second membrane, for various active forces, in Fig 6A. For a single membrane, the distance approaches a new equilibrium rapidly, $\sim 10^{-5}$ s. For an interface, Fig 6A demonstrates a rapid initial movement, $\sim 10^{-5}$ s, followed by a slower approach to the same equilibrium separation. In Fig 6B we explore this further by plotting the position of both membranes for $F = 10$ pN: We find that there is an initial rapid movement of the top membrane, i.e, the driven membrane (blue curve in B) $\sim 10^{-5}$ s, however this is accompanied by a rapid depression of the bottom membrane, i.e., the passive (red curve). Then, on a slower timescale $\sim 10^{-3}$ s, the passive membrane returns. We attribute the rapid depression to the incompressibility of the extracellular fluid, and the slow timescale to the thin-layer timescale identified above, as the excess fluid must drain from the interface.

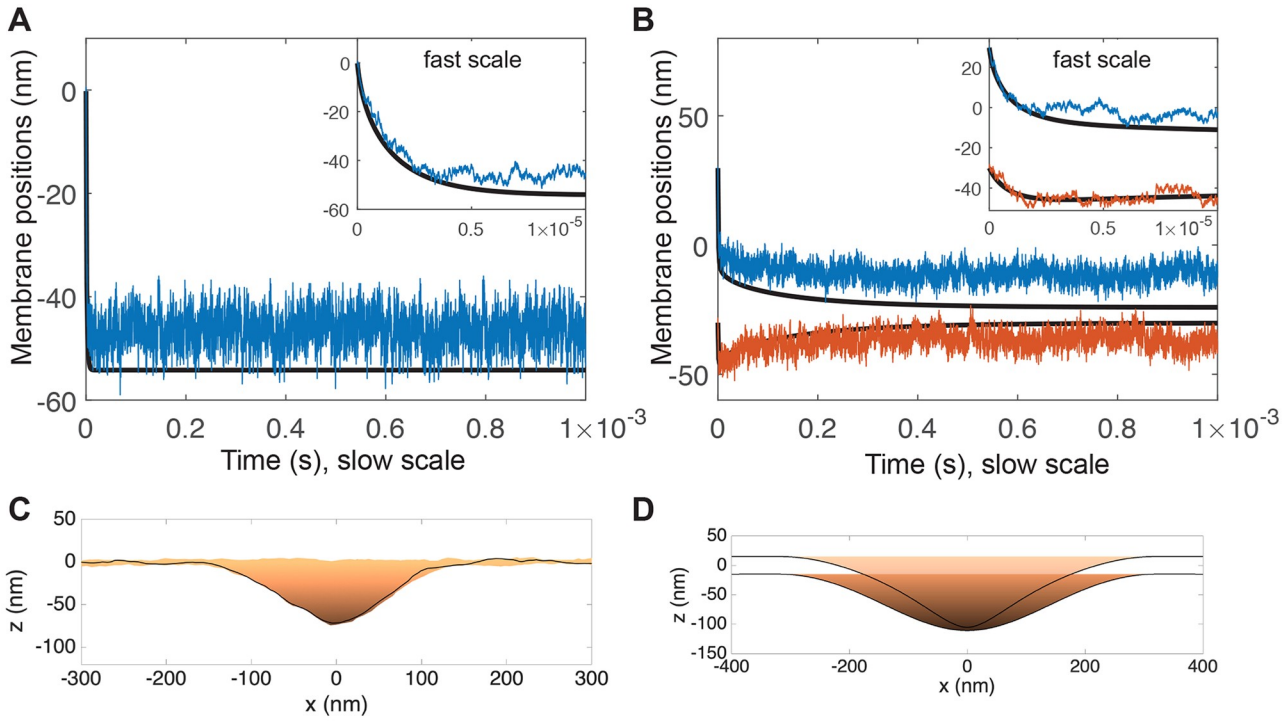

Fig 5. Active forces driving membrane proximity. (A) Active force of $F = 20$ pN applied to single membrane. Simulations including thermal undulations (blue) compared to purely deterministic simulations without thermal undulations. Inset shows fast timescale of mechanical equilibration. (B) Active force of $F = 20$ pN applied to top membrane at a cell-cell interface held apart $\Delta z_\infty = 50$ nm. After rapid initial phase (inset), equilibrium separation is not reached until $\sim 10^{-3}$ s. Parameters used in this simulation are $r_{\text{cell}} = 1$ μm, $r_{\text{free}} = 150$ nm, $\sigma_0 = 100$ pN/ μm. (C) Snapshot of equilibrium from single-membrane simulation with thermal fluctuations. (D) Snapshot of intermediate configuration at $t = 10^{-4}$ s from interface simulation without thermal fluctuations.

https://doi.org/10.1371/journal.pcbi.1006352.g005

Influence of membrane tension and surface organization of nonspecific adhesion molecules

The plasma membrane is under tension, maintained by hydrostatic pressure and regulation of exocytosis, endocytosis and membrane ruffles [40, 53] and is in the range of 3 – 300 pN/ μm [40, 41] and is spatially nonuniform [54]. We apply membrane tension in our simulation as a boundary surface tension with magnitude σ_0. We find that higher surface tension necessitates more force for the equivalent equilibrium displacement, as shown in Fig 7A. This demonstrates that the system is above the critical length scale below which surface tension is insignificant compared to membrane bending [17, 55]. Note that these these data show the equilibrium position in response to a constant force, therefore there is no effect of fluid dynamics, and thus no thin-layer effect.

The results we report are sensitive to the properties of the large surface molecule, such as the size of the region r_{free} around the receptor that is free of these molecules. To put this parameter in a form more readily comparable with molecular surface densities, we define the parameter $\rho = 1/r_{\text{free}}^2$, which has units of nm^{-2}. We previously estimated that receptor-ligand contact occurs in depletion zones with $r_{\text{free}} \sim 100$ nm [6]. In Fig 7B, we explore the equilibrium separation as a function of force for various surface densities, $r_{\text{free}} = 80$ nm($\rho = 1.6 \times 10^{-4}$ nm^{-2}), $r_{\text{free}} = 150$ nm($\rho = 4.4 \times 10^{-5}$ nm^{-2}, $r_{\text{free}} = 300$ nm($\rho = 1.1 \times 10^{-5}$ nm^{-2}. As expected, higher density of surface molecules reduces the equilibrium displacement.

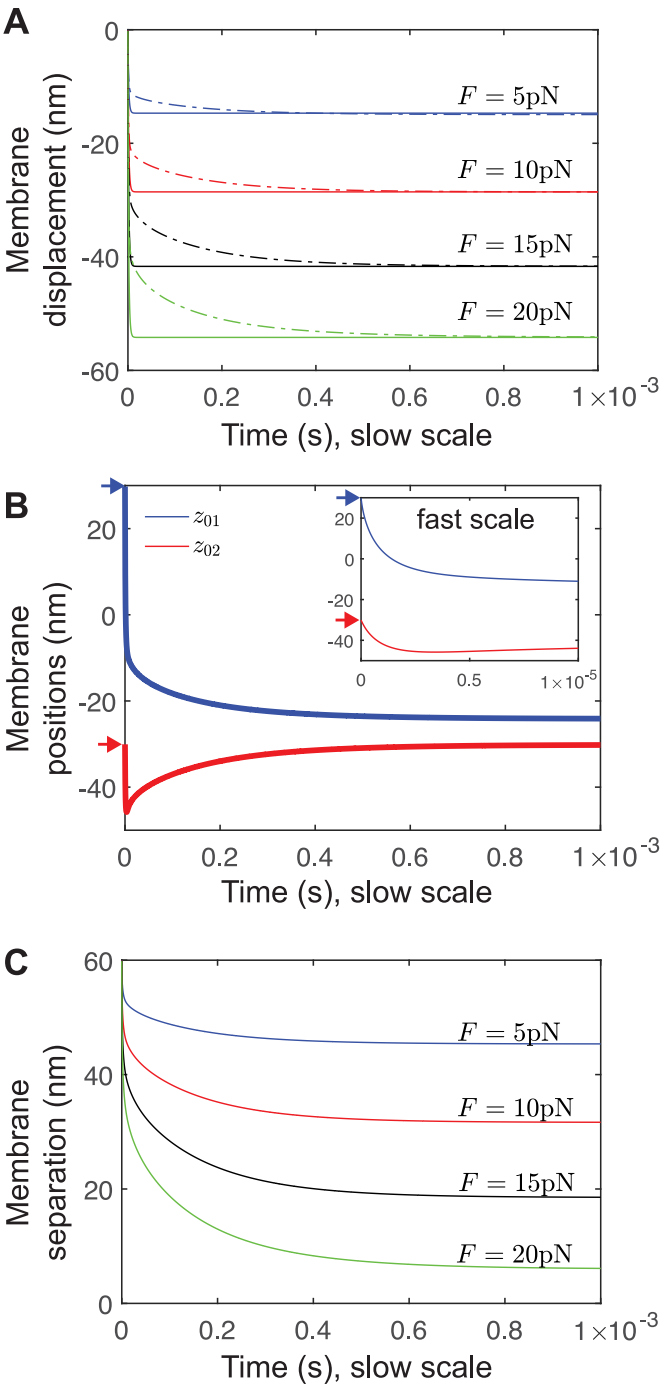

Fig 6. Active forces at a cell-cell interface exhibit a slow timescale of equilibration due to thin-layer effect. (A) Membrane displacement for various forces for a single membrane (solid curves), and the top membrane at an interface (dashed curves). (B) Membrane positions for $F = 10$ pN. The top membrane (blue) moves in an manner initially similar to the single-membrane case (inset), while the bottom membrane (red) is pushed away by hydrodynamic interaction. Then, on the slow timescale, the bottom membrane moves back up towards its equilibrium. Arrows indicate initial positions, to highlight the rapid initial movement otherwise difficult to see. (C) Membrane separation (which, in contrast to membrane displacement in (A), includes the slow return of the bottom membrane) for various forces. Thermal fluctuations are omitted in this figure.

https://doi.org/10.1371/journal.pcbi.1006352.g006

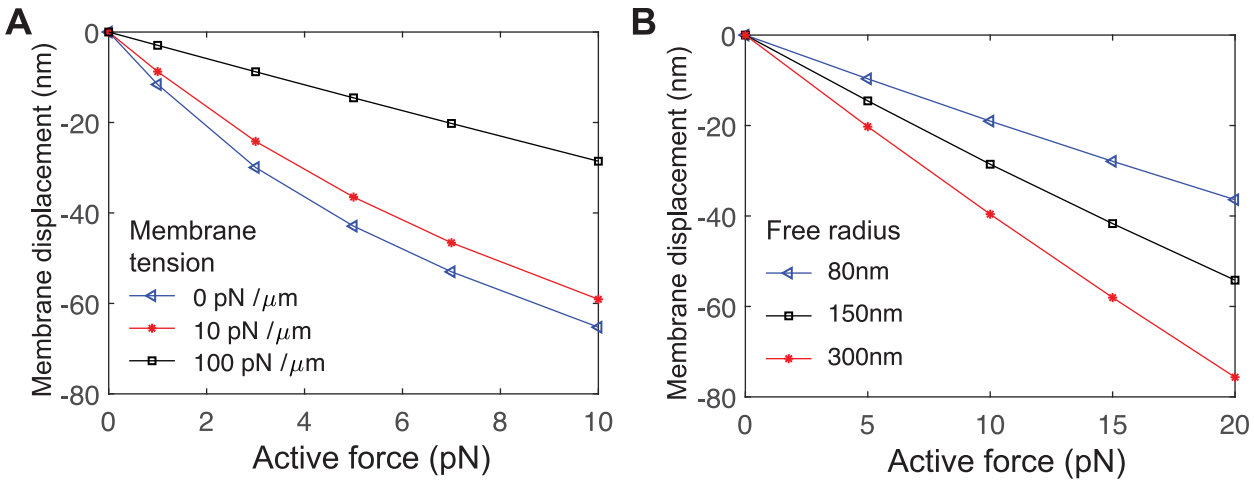

Fig 7. Equilibrium membrane displacement as a function of active force. (A) For various surface densities of non-specific adhesion molecules ρ, which relates to the free radius near the receptor r_{free} by $\rho \sim 1/r_{\text{free}}^2$. (B) For various values of membrane tension σ_0, applied at the boundary of both cells. Note since these data are at equilibrium, there is no thin-layer effect, and membrane separation is far-field separation minus membrane displacement. Further, since there is still nonzero separation from the second membrane, the presence of the second membrane does not influence the results. Thermal fluctuations are omitted throughout this figure.

https://doi.org/10.1371/journal.pcbi.1006352.g007

Optimal distance away from the target cell for active extension

The results we report are also sensitive to the molecular size Δz_∞ of the large surface molecule. The large range of estimates for Δz_∞ arises from the uncertainty about which molecules dominate the process of keeping the membranes apart. Molecules like CD45 may sterically maintain membrane separation by as little as 22nm. Non-specific adhesion molecules like LFA-ICAM and cadherins are estimated to span a range from 28nm [31] to 43nm [32, 33]. Estimates for the thickness of the glycocalyx range from 40 − 50 nm [34, 35] to 150 nm [36, 37]. So, we explore receptor proximity driven by active forces, varying the far-field separation Δz_∞ from 30nm to 120nm in Fig 8. To clarity, as with previous simulations, the majority of the membranes (everything outside the radius r_{free}) are held apart at a fixed distance Δz_∞. From this fixed distance, an active protrusion is extended from one membrane towards the other. We examine the time dynamics of the protrusion.

As the starting distance is increased, the time before proximity $\Delta z_0 < \Delta z_0^\star$ increases, shown in Fig 7B. However, we find that above a critical far-field separation $\Delta z_\infty \approx 80$ nm, membrane deformation speed increases, even though force is kept constant at $F = 10$ pN. The effect is modest but sufficient so that, over a large range of far-field separations ∼60 − 130 nm, the time to proximity does not increase for increasing separation, Fig 7C. Heuristically, this plateau arises because of a significant thin-layer effect dominates motion. Since this effect depends sensitively on the thickness of the thin layer, increasing the thickness reduces the effect, and the active protrusion can push more easily through the free fluid. On the other hand, although speed increases, the distance to the target cell also increases. Thus there is an optimal "attack distance" from which to extend a protrusion.

Membrane permeability value for which thermal and active proximity is accelerated

If a membrane were perfectly water permeable $\psi = \infty$ there would be no thin-layer effect. Biological membranes are sufficiently permeable that, in fast motile cells, fluid velocity appears

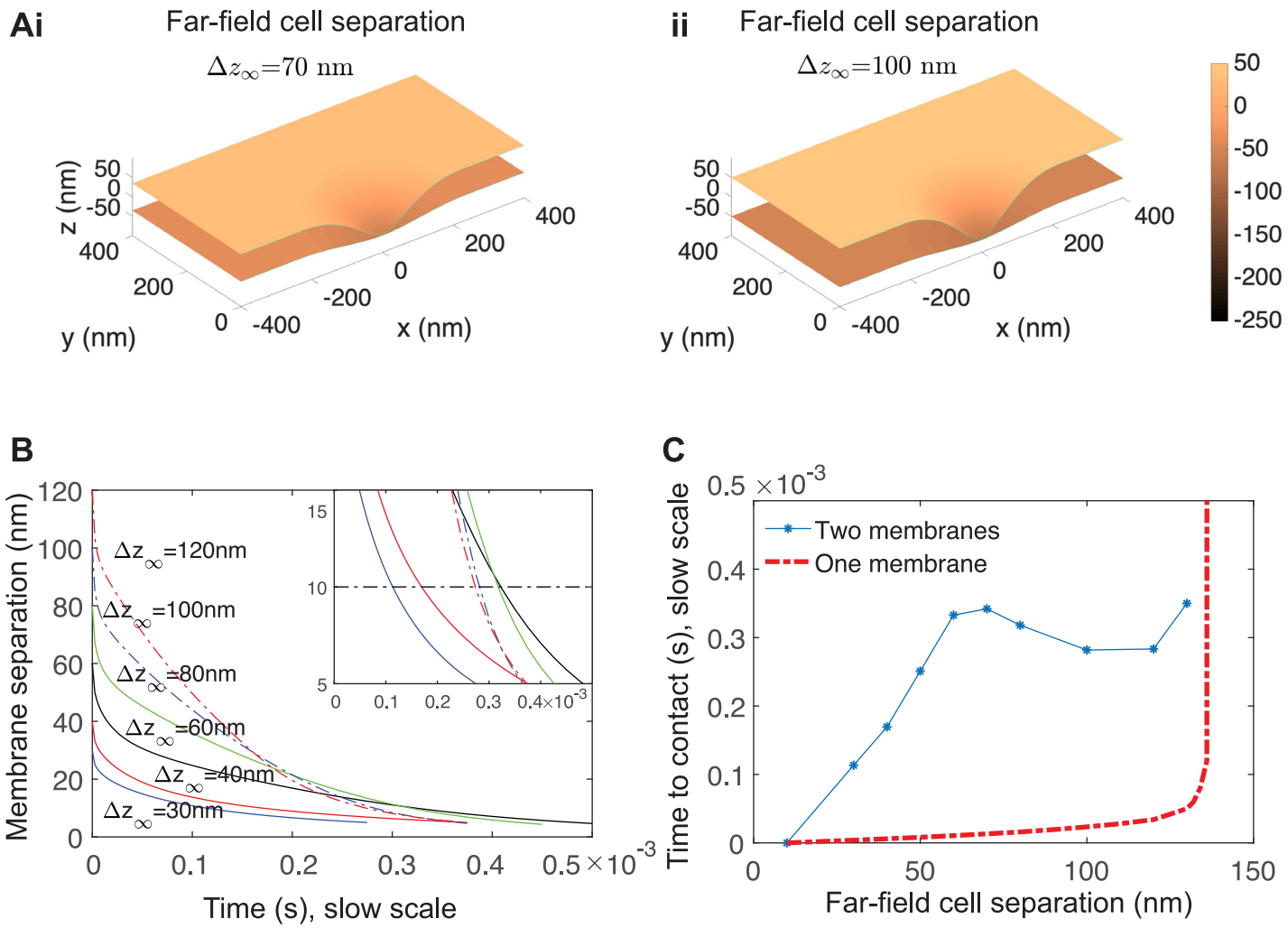

Fig 8. Active force of 10 pN for various initial cell separation distances demonstrates an optimal initial distance. (A) Snapshot of simulations with far-field separation Δz_∞ = 70nm and Δz_∞ = 100nm. Parameters used for both are r_{cell} = 1 μm (for clarity the full simulation domain is not show), r_{free} = 200 nm, σ_0 = 0. At these parameters, this force is sufficient to drive $\Delta z < 10$nm. (B) Membrane separation for various far-field separation Δz_∞. Inset shows non-monotonic behavior where the time series cross. (C) Time until $\Delta z < 10$nm versus far-field separation (blue asterisks). Simulations for a single membrane are shown (red, dashed) for comparison. The single-membrane time diverges around 140nm since this force induces an equilibrium deformation of that magnitude (Fig 7).

https://doi.org/10.1371/journal.pcbi.1006352.g008

stationary in the lab frame of reference when myosin contractility is inhibited [19]. Therefore, it is a priori reasonable to expect that there is a magnitude of permeability above which the slow-timescale behavior of the interface is removed, leaving only fast dynamics. We repeat the active force simulations at F = 20 pN, and explore permeabilities at each order of magnitude, in Fig 9. We find that the first significant deviation from impermeability ($\psi = 0$) occurs at $\psi \sim 10^2$ nm/sPa (red dotted). By $\psi = 10^4$ nm/sPa, the top membrane time series is comparable to the single-membrane case (Fig 6B), i.e., very little thin-layer effect is observed. The transition to fast-only dynamics occurs through a reduction in timescale, and only a weak reduction in amplitude (green curve is compressed horizontally).

Previous theoretical studies [22, 23] have estimated the parameter regimes in which permeation (i.e., flow across membranes) will dominate parallel flows (i.e., flow parallel to the interface). Specifically, [22] finds that the critical scale of permeability, above which permeation is

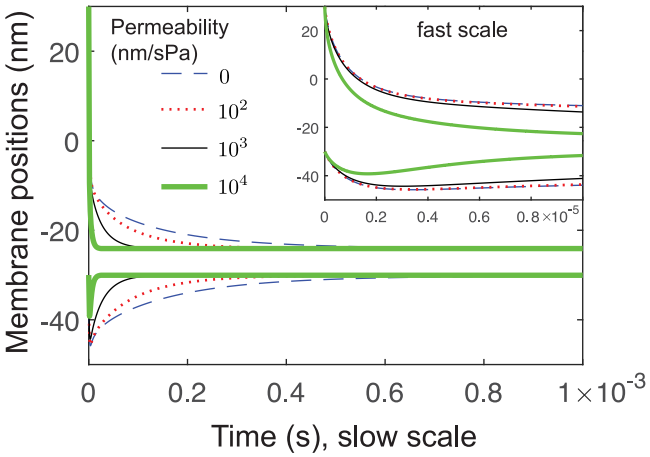

Fig 9. Influence of membrane permeability on thin-layer effect. Membrane positions are shown for $F = 10$ pN. For zero permeability (blue dashed), there is significant thin-layer effect. Significant changes to the time series are first seen for permeability $\psi = 10^2$ nm/sPa (red dotted). By permeability $\psi = 10^4$ nm/sPa, the top membrane time series is comparable to the single-membrane case (Fig 6B). Thermal fluctuations are omitted here.

https://doi.org/10.1371/journal.pcbi.1006352.g009

dominant, is

$$\psi \sim \frac{(\Delta z_\infty)^3}{\eta (r_{\text{free}})^2} \sim 10^4 \,\text{nm/ s Pa} \tag{2}$$

where we have changed their equation to our notation, and assumed that the dominant wavelength is $\sim (1/r_{\text{free}})$. This scaling is in agreement with our simulations.

Moreover, this is orders of magnitude larger than the permeability estimates10^{-2} nm/sPa [38]. The largest indirect estimates from motile epithelial keratocytes gives $\sim 10^1$ nm/sPa [19]. So, taken together, our results suggest the thin-layer effect cannot be abrogated by physiological levels of permeability.

Discussion

Fluid dynamics plays a role in cellular processes like the swimming of eukaryotes and bacteria, ciliary beating [56], and cell blebbing [57, 58], but also in less obvious examples like nuclear shape [59], organelle positioning [60, 61], some surface crawling of both eukaryotes [62] and bacteria [63], and ultra-fast endocytosis in neurons [64]. This work studies fluid dynamic effects in the context of transient cell-cell contact by immune cells [11, 13]. We find that thermal undulations are modified by the thin-layer effect, and this modification is primarily in their timescale, but not amplitude, in agreement with previous experimental work [11]. We find active forces of the magnitude present in cells ($\sim$10 pN) are sufficiently fast to drive sub-second receptor-ligand contact, although there is still an observable slow-down. And finally, we find that physiological levels of membrane permeability do not significantly change this.

Active protrusive forces like filopodia and microvilli are abundant in cells including naive, resting and activated T cells [37, 52]. However, in vitro reconstitutions in which two cell-sized lipid vesicles are brought into proximity [10] do not have active protrusion. Our simulations without active protrusion (Fig 3) predicts significant delay before the first reports of receptor-ligand contact. Interestingly, in vitro reconstitution take approximately 16 minutes before signs of molecular binding [10]. Our work suggests a source of this delay is the long timescale of fluctuations due to the thin layer: Hydrodynamics in the interface between vesicles is slow,

and in the total absence of active protrusion, receptor proximity must rely on thermal fluctuations hampered by the thin-layer effect.

For cells with active protrusions, our results suggest that the thin-layer effect can be readily overcome by the typical forces of filopodia [17, 18]. In our model, a constant force is maintained by the protrusive machinery as the membrane is driven outward, implicitly assuming that hydrodynamic drag is the rate-limiting process. Protrusions driven by polymerization of F-actin must assemble monomers at the leading edge, a process which can drive protrusions at 200 − 300nm/ s [17, 19], speeds that could produce proximity from a separation distance of $\Delta z_\infty = 50$nm in $\sim 10^{-1}$ s. The hydrodynamic-limited case we explore here produces close-contact at this distance in $\sim 10^{-3}$ s, suggesting that hydrodynamics is not rate-limiting. However, we note that our simulations assumed both the cytosolic and extracellular viscosities are that of water, $\eta = 10^{-3}$ Pas. This is a conservative estimate compared to established measurements of cytosolic viscosity that are one or two orders of magnitude larger [38]. Repeating our simulations with a change in viscosity would linearly scale all times, so a tenfold increase in viscosity would slow contact by tenfold. In this case, it is possible that hydrodynamics becomes limiting.

The slow timescale of hydrodynamic relaxation could explain the appearance of secretory clefts [65], long-lived blisters of extracellular fluid that are hypothesized to be particularly important for cytotoxic T cell function, since they ensure cytolytic granules secreted by the T cell are concentrated near the target cell [3, 66]. These blisters may arise and persist out-of-equilibrium due to the long-timescale of fluid evacuation through the tight cell-cell contact regions. This would provide an example of a cell-biological structure arising as a consequence of simple fluid dynamics, upon which regulation occurs by structures like the microtubule organizing center [66, 67].

The current simulations omit several properties of cell membranes that have the potential to modify cell-cell contact. Lipid membranes interact via several mechanisms. At sufficiently small separation distances, there are solvation forces, electrostatic and van der Waals interactions directly between the lipids. We make the approximation that the (cell plasma) membranes in our simulation are sufficiently far that the only interactions are mediated by other molecules, in particular the receptor and ligand and the non-specific adhesion molecules. We also neglect the hydrostatic and osmotic pressure differences ($\sim$ 1kPa in mammalian cells [68]). Perhaps most significantly, the F-actin cortex and its adhesion with the plasma membrane plays a major role in membrane dynamics [58, 68, 69]. We expect that modulating cortex-membrane adhesion would allow us to simulate active protrusions that, at high adhesion, behave more like narrow, finger-like filopodia [17], while at low adhesion behave more like microvilli and invadopodia [37], which are rounder and wider [52]. A major opportunity provided by computational fluid dynamics studies, rather than, e.g., analytical approaches, is the feasibility of studying more realistic geometries with more molecular participants and the inclusion of more physicochemical phenomena.

Methods

Numerical implementation. We use the Stochastic Immersed Boundary Method, an extension of the Immersed Boundary Method [30] developed by Atzberger and coworkers [24, 27, 28]. The fluid has velocity field $\mathbf{u}$ parameterized by Eulerian coordinate $\mathbf{x} \in \mathcal{D}$. The immersed structure has configuration described by $\mathbf{X}$ and is parametrized by $s \in \mathcal{S}$ in the membrane domain $\mathcal{S}$. The equations of motion are

$$\rho \partial \mathbf{u}/\partial t = \eta \nabla^2 \mathbf{u} - \nabla p + \mathbf{f}_{total}, \quad (3)$$

$$\nabla \cdot \mathbf{u} = 0, \quad (4)$$

$$\Phi[\mathbf{X}] = \Phi_{bend}[\mathbf{X}] + \Phi_{tension}[\mathbf{X}] + \Phi_{shear}[\mathbf{X}], \tag{5}$$

$$\mathbf{F}_{mem} = -\frac{\delta\Phi[\mathbf{X}]}{\delta\mathbf{X}}, \tag{6}$$

$$\mathbf{f}_{total}(\mathbf{x},t) = \Lambda(\mathbf{F}_{mem} + \mathbf{F}_{ex}) + (\nabla_{\mathbf{x}}\cdot\Lambda)k_BT + \mathbf{g}_{thm}, \tag{7}$$

$$\frac{\partial\mathbf{X}}{\partial t} = \Gamma\mathbf{u} + \bar{\psi}(\mathbf{F}_{mem} + \mathbf{F}_{ex} + \mathbf{F}_{thm}). \tag{8}$$

The first term in Eq 3 is the inertial term, where ρ is the fluid mass density, which must be included to accommodate thermal fluctuations (even though simple scaling put the system in the low-Reynolds regime [26, 27]). The pressure p is imposed by the incompressiblity condition in Eq 4. The "external" forces $\mathbf{F}_{ex}$, include both the nonspecific adhesions and the active pushing force at the center of the membrane disk. The active force is applied to nodes within a disk of radius a at the center of the disk, which for most discretizations involves approximately 7 nodes (the same nodes throughout the simulation) so that the total force F_0 is distributed equally among the nodes. The nonspecific adhesions are placed on all nodes outside of the radius r_{free}. So, as r_{free} is changed for different simulations, the surface density of nonspecific adhesions is constant, and the number is changed.

The force from the membrane, Eq 6, is computed using a variational approach from the membrane energy. We describe the Helfrich energy functional [70] with bending energy

$$\Phi_{bend}(\mathbf{X}) = \frac{\kappa_B}{2}\int_{\mathcal{S}} H^2 dA, \tag{9}$$

where κ_B is bending rigidity and H is mean curvature of the membrane surface. In addition to the bending energy, we consider a membrane that resists area changes by a surface tension energy

$$\Phi_{tension}[\mathbf{X}] = \sigma_0\int_{\mathcal{S}}\left(\frac{dA - dA_0}{dA_0}\right)^2 dA_0 \tag{10}$$

where σ_0 is the surface tension constant. Finally, the membrane resists shear in order to maintain numerical stability [24]. Details of the shear term are described in the Supplemental Information. While this term is not meant to represent a physical restoring force in fluid membranes like the cell plasma membrane, we include it to enable our computational method to work efficiently without the need for, e.g., remeshing.

The fluid and structure are coupled by

$$(\Lambda\mathbf{F})(\mathbf{x},t) = \int_{\Omega}\mathbf{F}(\mathbf{q},t)\delta(\mathbf{x} - \mathbf{X}(\mathbf{q},t))d\mathbf{q}, \tag{11}$$

$$(\Gamma\mathbf{u})(\mathbf{q},t) = \int_{\Omega}\mathbf{u}(\mathbf{x},t)\delta(\mathbf{x} - \mathbf{X}(\mathbf{q},t))d\mathbf{x}. \tag{12}$$

The smoothing function δ is defined as [24, 29, 30]

$$\delta(\mathbf{x}) = \frac{1}{a^3}\varphi\left(\frac{|x|}{a}\right)\varphi\left(\frac{|y|}{a}\right)\varphi\left(\frac{|z|}{a}\right) \quad \text{for} \quad \mathbf{x} = (\mathrm{x},\mathrm{y},\mathrm{z}), \tag{13}$$

where

$$\varphi(r) = \begin{cases} \frac{1}{8}(3 - 2r + \sqrt{1 + 4r - 4r^2}) & \text{for} \quad 0 \leq r \leq 1, \\ \frac{1}{8}(5 - 2r - \sqrt{-7 + 12r - 4r^2}) & \text{for} \quad 1 < r \leq 2, \\ 0 & \text{for} \quad 2 < r \end{cases} \tag{14}$$

and $a = \Delta x$, thus making the support of the smoothing function comparable to the Eulerian discretization Δx.

Eq 8 describes the motion of the membrane, which follows the fluid velocity u but with a pressure-driven difference due to permeability, with coefficient $\bar{\psi}$. This coefficient assumes a linear relationship between velocity difference and force density (in, e.g., pN/ nm^3). It is related to the membrane surface permeability ψ, the relevant permeability measure for flow across a surface [19, 22, 23, 38] that connects velocity difference and pressure across the membrane by $\psi = \bar{\psi}/\Delta x$ where Δx is the spatial discretization of the fluid (Eulerian) domain. Note ψ (and $\bar{\psi}$) scale as the inverse of the permeability coefficient Y in [24]. Furthermore, ψ is related to the coefficient K_{Darcy} in Darcy's Law $\vec{v} = K_{\text{Darcy}} \nabla p/\eta$ by $\psi \approx K_{\text{Darcy}}\, w/\eta$ where w is the width of the membrane. As a validation of the permeability implementation, and of the correct conversion of permeability coefficients, we perform a test at fixed ψ with different pressure differences across the membrane, to verify that this leads proportional membrane velocities. This is located in Supporting Information.

The stochastic fields $\mathbf{F}_{\text{thm}}$ and $\mathbf{g}_{\text{thm}}$ satisfy the fluctuation-dissipation theorem [24, 28] are Gaussian random fields with mean zero and variance-covariance given by

$$\langle \mathbf{g}_{thm}(\mathbf{x}, s)\mathbf{g}^T_{thm}(\mathbf{x}', t)\rangle = 2k_B T\mu\Delta\delta(t - s)\delta(\mathbf{x} - \mathbf{x}'), \tag{15}$$

$$\langle \mathbf{F}_{thm}(\mathbf{X}, s)\mathbf{F}^T_{thm}(\mathbf{X}', t)\rangle = 2k_B T\psi^{-1}\delta(t - s)\delta(\mathbf{X} - \mathbf{X}'), \tag{16}$$

$$\langle \mathbf{F}_{thm}(\mathbf{X}, s)\mathbf{g}^T_{thm}(\mathbf{x}, t)\rangle = 0. \tag{17}$$

We use a spatial discretization for the fluid domain of Δx = 5nm and a time-stepping scheme with $\Delta t = 10^{-10}$ s. Further description of energy terms and details of numerical implementation are in the S1 Appendix.

Estimation of mean first-passage time. The receptor-site membrane distance Δz follows a stochastic trajectory. In the absence of deterministic forces, we find that, in the case of a single membrane, it is well-approximated by an Ornstein-Ulenbeck process [47] in the new variable $Z = \Delta z - \langle \Delta z \rangle$,

$$dZ = -\frac{1}{\tau} Z dt + \frac{\sigma}{\sqrt{\tau}} dW \tag{18}$$

where W is a Weiner process. This has stationary distribution

$$p(z) = \frac{1}{\sqrt{2\pi\sigma^2}} \exp\left(-\frac{z^2}{2\sigma^2}\right) \tag{19}$$

and autocorrelation function

$$\alpha(\delta t) = \exp\left(-\delta t/\tau\right). \tag{20}$$

For the case of an interface, we find that the receptor-site membrane-membrane distance Δz follows a stochastic trajectory with autocorrelation that is well-approximated by

$$\alpha(\delta t) \approx ce^{-\delta t/\tau_{\text{slow}}} + \sqrt{1-c^2}e^{-\delta t/\tau_{\text{fast}}}. \tag{21}$$

This is the autocorrelation function of a two-component OU process

$$dX = -\frac{1}{\tau_{\text{slow}}}Xdt + \frac{\sigma}{\sqrt{\tau_{\text{slow}}}}dW_1, \tag{22}$$

$$dY = -\frac{1}{\tau_{\text{fast}}}Ydt + \frac{\sigma}{\sqrt{\tau_{\text{fast}}}}dW_2, \tag{23}$$

$$Z = cX + \sqrt{1-c^2}Y, \tag{24}$$

where, without loss of generality, we assume the two hidden components X and Y have the same variance σ^2 (since any difference can be absorbed into c), and we define the fraction of the process attributed to the slow timescale c and fast timescale $\sqrt{1-c^2}$, again without loss of generality, as a convenient way of fitting the variance.

We refer to Eq 18 as the one-component OU process to describe a single membrane, and Eqs 22–24 as the two-component OU process to describe the interface. For both of these, we present methods for determining MFPTs in the S1 Appendix.

Supporting information

S1 Appendix. Supplemental methods. Description of computational fluid dynamics method and implementation. Numerical validation of thermal fluctuations and permeability. Description of weighted ensemble method and implementation.
(PDF)

Author Contributions

Conceptualization: Jay Newby, Elizabeth L. Read, John Lowengrub, Jun Allard.

Formal analysis: Kai Liu, Brian Chu, Elizabeth L. Read, Jun Allard.

Funding acquisition: Jay Newby, John Lowengrub, Jun Allard.

Investigation: Kai Liu, Brian Chu, Jun Allard.

Methodology: Kai Liu.

Software: Kai Liu.

Supervision: Jay Newby, Elizabeth L. Read, John Lowengrub, Jun Allard.

Validation: Brian Chu.

Visualization: Kai Liu, Brian Chu, Elizabeth L. Read, Jun Allard.

Writing – original draft: Kai Liu, Elizabeth L. Read, Jun Allard.

Writing – review & editing: Kai Liu, Elizabeth L. Read, Jun Allard.

References

1. Ng MR, Besser A, Brugge JS, Danuser G. Mapping the dynamics of force transduction at cell-cell junctions of epithelial clusters. eLife. 2014; 3:e03282. https://doi.org/10.7554/eLife.03282 PMID: 25479385

2. Bambardekar K, Clément R, Blanc O, Chardès C, Lenne PF. Direct laser manipulation reveals the mechanics of cell contacts in vivo. Proc Natl Acad Sci USA. 2015; 112(5):1416–1421. https://doi.org/10.1073/pnas.1418732112 PMID: 25605934
3. de la Roche M, Asano Y, Griffiths GM. Origins of the cytolytic synapse. Nat Rev Immunol. 2016; 16 (7):421–432. https://doi.org/10.1038/nri.2016.54 PMID: 27265595
4. Van Der Merwe PA, Dushek O. Mechanisms for T cell receptor triggering. Nat Rev Immunol. 2010; 11 (1):47–55. https://doi.org/10.1038/nri2887 PMID: 21127503
5. Rozycki B, Lipowsky R, Weikl TR. Segregation of receptor-ligand complexes in cell adhesion zones: phase diagrams and the role of thermal membrane roughness. New J Phys. 2010; 12(9):095003. https://doi.org/10.1088/1367-2630/12/9/095003
6. Allard JF, Dushek O, Coombs D, Van Der Merwe PA. Mechanical Modulation of Receptor-Ligand Interactions at Cell-Cell Interfaces. Biophys J. 2012; 102(6):1265–1273. https://doi.org/10.1016/j.bpj.2012.02.006 PMID: 22455909
7. Chang VT, Fernandes RA, Ganzinger KA, Lee SF, Siebold C, McColl J, et al. Initiation of T cell signaling by CD45 segregation at'close contacts'. Nat Immunol. 2016; 17(5):574–582. https://doi.org/10.1038/ni.3392 PMID: 26998761
8. Schmid EM, Bakalar MH, Choudhuri K, Weichsel J, Ann HS, Geissler PL, et al. Size-dependent protein segregation at membrane interfaces. Nat Phys. 2016; p. 1–10.
9. Yakovian O, Schwarzer R, Sajman J, Neve-Oz Y, Razvag Y, Herrmann A, et al. Gp41 dynamically interacts with the TCR in the immune synapse and promotes early T cell activation. Sci Rep. 2018; 8(1):1–16. https://doi.org/10.1038/s41598-018-28114-5
10. Carbone CB, Kern N, Fernandes RA, Hui E, Su X, Garcia KC, et al. In vitro reconstitution of T cell receptor-mediated segregation of the CD45 phosphatase. Proc Natl Acad Sci USA. 2017; 114(44):E9338–E9345. https://doi.org/10.1073/pnas.1710358114 PMID: 29042512
11. Kaizuka Y, Groves JT. Hydrodynamic Damping of Membrane Thermal Fluctuations near Surfaces Imaged by Fluorescence Interference Microscopy. Phys Rev Lett. 2006; 96(11):1035–4. https://doi.org/10.1103/PhysRevLett.96.118101
12. Lin LCL, Groves JT, Brown FLH. Analysis of Shape, Fluctuations, and Dynamics in Intermembrane Junctions. Biophys J. 2006; 91(10):3600–3606. https://doi.org/10.1529/biophysj.106.091843 PMID: 16920837
13. Carlson A, Mahadevan L. Elastohydrodynamics and Kinetics of Protein Patterning in the Immunological Synapse. PLoS Comp Biol. 2015; 11(12):e1004481–16. https://doi.org/10.1371/journal.pcbi.1004481
14. Mani M, Gopinath A, Mahadevan L. How Things Get Stuck: Kinetics, Elastohydrodynamics, and Soft Adhesion. Phys Rev Lett. 2012; 108(22). https://doi.org/10.1103/PhysRevLett.108.226104 PMID: 23003628
15. Vázquez-Quesada A, Ellero M. Analytical solution for the lubrication force between two spheres in a bi-viscous fluid. Phys Fluids. 2016; 28(7):073101–20. https://doi.org/10.1063/1.4954815
16. Barnocky G, Flow RDIJoM, 1989. The lubrication force between spherical drops, bubbles and rigid particles in a viscous fluid. Int J Multiphase Flow. 1989; 15(4):627–638. https://doi.org/10.1016/0301-9322(89)90057-8
17. Atilgan E, Wirtz D, Sun SX. Mechanics and dynamics of actin-driven thin membrane protrusions. Biophys J. 2006; 90(1):65–76. https://doi.org/10.1529/biophysj.105.071480 PMID: 16214866
18. Footer MJ, Kerssemakers JWJ, Theriot JA, Dogterom M. Direct Measurement of Force Generation by Actin Filament Polymerization Using an Optical Trap. Proc Natl Acad Sci 2007; 104(7)2181–2186. https://doi.org/10.1073/pnas.0607052104 PMID: 17277076
19. Keren K, Yam PT, Kinkhabwala A, Mogilner A, Theriot JA. Intracellular fluid flow in rapidly moving cells. Nat Cell Biol. 2009; 11(10):1219–1224. https://doi.org/10.1038/ncb1965 PMID: 19767741
20. Li W, Jin WW, Tsuji K, Chen Y, Nomura N, Su L, et al. Direct interaction of ezrin and AQP2 and its role in AQP2 trafficking. J Cell Sci. 2017; 130:2914–2925.
21. Papadopoulos MC, Hara-Chikuma M, Verkman AS. Impairment of angiogenesis and cell migration by targeted aquaporin-1 gene disruption. Nature. 2005; 434:786–792. https://doi.org/10.1038/nature03460 PMID: 15815633
22. Gov N, Zilman AG, Safran S. Hydrodynamics of confined membranes. Phy Rev E. 2004; 70(1):1035–10. https://doi.org/10.1103/PhysRevE.70.011104
23. Prost J, Manneville JB, Bruinsma R. Fluctuation-magnification of non-equilibrium membranes near a wall. Eur Phys J B. 1998; 1(4):465–480. https://doi.org/10.1007/s100510050209

24. Wu CH, Fai TG, Atzberger PJ, Peskin CS. Simulation of Osmotic Swelling by the Stochastic Immersed Boundary Method. SIAM J Scientific Computing. 2015; 37(4):B660–B688. https://doi.org/10.1137/14098404X

25. Brown FLH. Elastic Modeling of Biomembranes and Lipid Bilayers. Annu Rev Phys Chem. 2008; 59 (1):685–712. https://doi.org/10.1146/annurev.physchem.59.032607.093550 PMID: 18173377

26. Liu K, Lowengrub J, Allard J. Efficient simulation of thermally fluctuating biopolymers immersed in fluids on 1-micron, 1-second scales; J Comp Phys, accepted 2019

27. Atzberger PJ. A note on the correspondence of an immersed boundary method incorporating thermal fluctuations with Stokesian-Brownian dynamics. Physica D. 2007; 226:144–150. https://doi.org/10.1016/j.physd.2006.11.013

28. Atzberger P. Stochastic Eulerian Lagrangian methods for fluid structure interactions with thermal fluctuations. J Comp Phys. 2011; 230:2821–2837. https://doi.org/10.1016/j.jcp.2010.12.028

29. Atzberger P. A stochastic immersed boundary method for fluid-structure dynamics at microscopic length scales. J Comp Phys 224 (2007)1255–1292.

30. Peskin CS. The Immersed Boundary Method. Acta Numerica. 2002; p. 479–517.

31. Biswas KH, Groves JT. A Microbead Supported Membrane-Based Fluorescence Imaging Assay Reveals Intermembrane Receptor–Ligand Complex Dimension with Nanometer Precision. Langmuir. 2016; 32(26):6775–6780. https://doi.org/10.1021/acs.langmuir.6b01377 PMID: 27264296

32. Monks CR, Freiberg BA, Kupfer H, Sciaky N, Kupfer A. Three-dimensional segregation of supramolecular activation clusters in T cells. Nature. 1998; 395(6697):82–86. https://doi.org/10.1038/25764 PMID: 9738502

33. Qi SY, Groves JT, Chakraborty AK. Synaptic pattern formation during cellular recognition. Proc Natl Acad Sci USA. 2001; 98(12):6548–6553. https://doi.org/10.1073/pnas.111536798 PMID: 11371622

34. Soler M, Desplat-Jego S, Vacher B, Ponsonnet L, Fraterno M, Bongrand P, et al. Adhesion-related glycocalyx study: quantitative approach with imaging-spectrum in the energy filtering transmission electron microscope (EFTEM). FEBS Letters. 1998; 429(1):89–94. https://doi.org/10.1016/S0014-5793(98)00570-5 PMID: 9657389

35. Paszek MJ, Boettiger D, Weaver VM, Hammer DA. Integrin Clustering Is Driven by Mechanical Resistance from the Glycocalyx and the Substrate. PLoS Comp Biol. 2009; 5(12):e1000604. https://doi.org/10.1371/journal.pcbi.1000604

36. Squire JM, Chew M, Nneji G, Neal C, Barry J, Michel C. Quasi-Periodic Substructure in the Microvessel Endothelial Glycocalyx: A Possible Explanation for Molecular Filtering? J Structural Biol. 2001; 136 (3):239–255. https://doi.org/10.1006/jsbi.2002.4441

37. Sage PT, Varghese LM, Martinelli R, Sciuto TE, Kamei M, Dvorak AM, et al. Antigen Recognition Is Facilitated by Invadosome-like Protrusions Formed by Memory/Effector T Cells. J Immunol. 2012; 188 (8):3686–3699. https://doi.org/10.4049/jimmunol.1102594 PMID: 22442443

38. Mogilner A, Manhart A. Intracellular Fluid Mechanics: Coupling Cytoplasmic Flow with Active Cytoskeletal Gel. Annu Rev Fluid Mech. 2018; 50(1):347–370. https://doi.org/10.1146/annurev-fluid-010816-060238

39. Choudhuri K, Wiseman D, Brown MH, Gould K, Van Der Merwe PA. T-cell receptor triggering is critically dependent on the dimensions of its peptide-MHC ligand. Nat Cell Biol. 2005; 436(7050):578–582.

40. Sens P, Plastino J. Membrane tension and cytoskeleton organization in cell motility. J Phys Cond Mat. 2015; 27(27):1–13. https://doi.org/10.1088/0953-8984/27/27/273103

41. Lieber AD, Yehudai-Resheff S, Barnhart EL, Theriot JA, Keren K. Membrane Tension in Rapidly Moving Cells Is Determined by Cytoskeletal Forces. Curr Biol. 2013; 23(15):1409–1417. https://doi.org/10.1016/j.cub.2013.05.063 PMID: 23831292

42. Pollard TD, Cooper JA. Actin, a Central Player in Cell Shape and Movement. Science. 2009; 326 (5957):1208–1212. https://doi.org/10.1126/science.1175862 PMID: 19965462

43. Aratyn-Schaus Y, Gardel ML. Transient Frictional Slip between Integrin and the ECM in Focal Adhesions under Myosin II Tension. Curr Biol. 2010; 20(13):1145–1153. https://doi.org/10.1016/j.cub.2010.05.049 PMID: 20541412

44. Maruthamuthu V, Sabass B, Schwarz US, Gardel ML. Cell-ECM traction force modulates endogenous tension at cell-cell contacts. Proc Natl Acad Sci USA. 2011; 108(12):–4713. https://doi.org/10.1073/pnas.1011123108

45. Netz RR, Lipowsky R. Stacks of Fluid Membranes under Pressure and Tension. Euro Phys Lett. 2007; 29(4):345–350. https://doi.org/10.1209/0295-5075/29/4/013

46. Freund LB. Entropic pressure between biomembranes in a periodic stack due to thermal fluctuations. Proc Natl Acad Sci USA. 2013; 110(6):2047–2051. https://doi.org/10.1073/pnas.1220968110 PMID: 23277559

47. Gardiner C. Handbook of Stochastic Methods. 4th ed. Springer; 2009.

48. Zuckerman DM, Chong LT. Weighted Ensemble Simulation: Review of Methodology, Applications, and Software. Annu Rev Biophysics. 2017; 46(1):43–57. https://doi.org/10.1146/annurev-biophys-070816-033834

49. Tse MJ, Chu BK, Roy M, Read EL. DNA-Binding Kinetics Determines the Mechanism of Noise-Induced Switching in Gene Networks. Biophys J. 2015; 109(8):1746–1757. https://doi.org/10.1016/j.bpj.2015.08.035 PMID: 26488666

50. Thomas M. Some mean first-passage time approximations for the Ornstein-Uhlenbeck process. J Appl Prob. 1975; 13(1):183.

51. Leijnse N, Oddershede LB, Bendix PM. An updated look at actin dynamics in filopodia. Cytoskeleton. 2015; 72(2):71–79. https://doi.org/10.1002/cm.21216 PMID: 25786787

52. Jung Y, Riven I, Feigelson SW, Kartvelishvily E, Tohya K, Miyasaka M, et al. Three-dimensional localization of T-cell receptors in relation to microvilli using a combination of superresolution microscopies. Proc Natl Acad Sci USA. 2016; 113(40):E5916–E5924. https://doi.org/10.1073/pnas.1605399113 PMID: 27647916

53. Guillou L, Babataheri A, Saitakis M, Bohineust A, Dogniaux S, Hivroz C, et al. T-lymphocyte passive deformation is controlled by unfolding of membrane surface reservoirs. Mol Biol Cell. 2016; 27(22):3574–3582. https://doi.org/10.1091/mbc.E16-06-0414 PMID: 27605708

54. Fogelson B, Mogilner A. Computational estimates of membrane flow and tension gradient in motile cells. PLoS ONE. 2014;. https://doi.org/10.1371/journal.pone.0084524 PMID: 24465414

55. Bruinsma R, Behrisch A, Sackmann E. Adhesive switching of membranes: experiment and theory. Phys Rev E. 2000; 61(4 Pt B):4253–4267. https://doi.org/10.1103/PhysRevE.61.4253

56. Guirao B, Meunier A, Mortaud S, Aguilar A, Corsi JM, Strehl L, et al. Coupling between hydrodynamic forces and planar cell polarity orients mammalian motile cilia. Nature. 2010; 12(4):341–350.

57. Tinevez JY, Schulze U, Salbreux G, Roensch J, Joanny JF, Paluch E. Role of cortical tension in bleb growth. Proc Natl Acad Sci USA. 2009; 106(44):18581–18586. https://doi.org/10.1073/pnas.0903353106 PMID: 19846787

58. Manakova K, Yan H, Lowengrub J, Allard J. Cell Surface Mechanochemistry and the Determinants of Bleb Formation, Healing, and Travel Velocity. Biophys J. 2016; 110(7):1636–1647. https://doi.org/10.1016/j.bpj.2016.03.008 PMID: 27074688

59. Kim DH, Li B, Si F, Phillip JM, Wirtz D, Sun SX. Volume regulation and shape bifurcation in the cell nucleus. J Cell Sci. 2015; 128(18):3375–3385. https://doi.org/10.1242/jcs.166330 PMID: 26243474

60. Yi K, Unruh JR, Deng M, Slaughter BD, Rubinstein B, Li R. Dynamic maintenance of asymmetric meiotic spindle position through Arp2/3-complex-driven cytoplasmic streaming in mouse oocytes. Nat Cell Biol. 2011; 13(10):1252–1258. https://doi.org/10.1038/ncb2320 PMID: 21874009

61. Nazockdast E. Cytoplasmic flows as signatures for the mechanics of mitotic positioning. Mol Biol Cell. 2017; 28(23):3133–3470. https://doi.org/10.1091/mbc.e16-02-0108

62. Bergert M, Erzberger A, Desai RA, Aspalter IM, Oates AC, Charras G, et al. Force transmission during adhesion-independent migration. Nat Cell Biol. 2015; 17(4):524–529. https://doi.org/10.1038/ncb3134 PMID: 25774834

63. Siryaporn A, Kim MK, Shen Y, Stone HA, Gitai Z. Colonization, Competition, and Dispersal of Pathogens in Fluid Flow Networks. Curr Biol. 2015; 25(9):1201–1207. https://doi.org/10.1016/j.cub.2015.02.074 PMID: 25843031

64. Lowengrub J, Allard J, Aland S. Numerical simulation of endocytosis: Viscous flow driven by membranes with non-uniformly distributed curvature-inducing molecules. J Comp Phys. 2016; 309(C):112–128. https://doi.org/10.1016/j.jcp.2015.12.055

65. Jenkins MR, Stinchcombe JC, Au-Yeung BB, Asano Y, Ritter AT, Weiss A, et al. Distinct structural and catalytic roles for Zap70 in formation of the immunological synapse in CTL. eLife. 2014; 3:947–21. https://doi.org/10.7554/eLife.01310

66. Stinchcombe JC, Griffiths GM. Secretory Mechanisms in Cell-Mediated Cytotoxicity. Annu Rev Cell and Dev Biol. 2007; 23(1):495–517. https://doi.org/10.1146/annurev.cellbio.23.090506.123521

67. Ritter AT, Asano Y, Stinchcombe JC, Dieckmann NMG, Chen BC, Gawden-Bone C, et al. Actin Depletion Initiates Events Leading to Granule Secretion at the Immunological Synapse. Immunity. 2015; 42(5):864–876. https://doi.org/10.1016/j.immuni.2015.04.013 PMID: 25992860

68. Tao J, Sun SX. Active Biochemical Regulation of Cell Volume and a Simple Model of Cell Tension Response. Biophys J. 2015; 109(8):1541–1550. https://doi.org/10.1016/j.bpj.2015.08.025 PMID: 26488645

69. Clark AG, Dierkes K, Paluch EK. Monitoring Actin Cortex Thickness in Live Cells. Biophys J. 2013; 105 (3):570–580. https://doi.org/10.1016/j.bpj.2013.05.057 PMID: 23931305

70. Helfrich W. Elastic properties of lipid bilayers: theory and possible experiments. Z Naturf C. 1973; 28:693–703. https://doi.org/10.1515/znc-1973-11-1209